Optically enhancing and controlling photoacoustic signals using ultra-thin semiconductor coatings on metal surfaces

KOMAL CHAUDHARY, MAKSYM ILLIENKO, THOMAS VAN DEN HOOVEN, [iD] STEFAN WITTE, [iD] AND PAUL PLANKEN* [iD]

Advanced Research Center for Nanolithography (ARCNL), Science Park 106, 1098 XG Amsterdam, The Netherlands
*planken@arcnl.nl

Abstract: We present a simple approach to enhance the signal strength and detection sensitivity of weak photoacoustic signals, by using ultrathin, high refractive index, absorbing semiconductor layers on metal surfaces. They form etalon resonances with reflection minima already for layer thicknesses of only a few tens of nm. Strain waves induce changes in the physical/optical thickness of the layers and/or changes in the phase and amplitude of light upon reflection from the metal-semiconductor interface. When the reflection is optically probed near the steep slope of the etalon resonance as a function of semiconductor layer thickness, the optical response is enhanced. With a 12 nm thick Ge layer on Au, we observed a 15-fold increase in the absolute reflection changes induced by strain waves compared to the signal without the Ge layer. Moreover, thin semiconductor layers can be used as transducers, enabling the generation of higher-frequency strain waves in the metal where the layer thickness determines the spectrum of these waves. Additionally, by properly choosing the semiconductor thickness and the pump-probe wavelengths, increased control over where light is absorbed is obtained. This offers some flexibility in tailoring the light absorption in both the metal and the semiconductor. We demonstrate this with a Si layer on Pt, where at 800 nm pump wavelength, most light is absorbed by Pt, while at 400 nm, both Pt and Si absorb light. Our results show the potential of this approach to address the challenge of detecting weak photoacoustic signals and to provide some control over strain wave generation.

1. Introduction

Photoacoustics, the optical generation and detection of ultra-high frequency strain waves, combines the deep penetration of sound with high optical resolution, overcoming the limitations of traditional optical methods for inspection of opaque materials. The strain waves can be generated when ultrafast laser pulses are absorbed by a material, resulting in a localized temperature increase. This causes a thermo-elastic expansion and launches strain waves into the surrounding medium [1,2]. These strain waves can be detected by measuring the changes in optical properties of the medium, either in reflection, transmission, or by diffraction [3–5]. Photoacoustics has many applications, such as photoacoustic imaging [6–8], photoacoustic spectroscopy [9,10], material characterization [11–15], the study of electron dynamics [16,17], the generation of terahertz radiation [18] and the detection of buried structures [19–21]. Furthermore, for high-resolution applications, photoacoustic transducers are also crucial and often require advancements in material and device technology to effectively operate at high ultrasonic frequencies [22,23].

Despite their widespread applicability, photoacoustic measurements are challenging, as signals are generally weak. This arises from two primary problems. Firstly, weak absorption of light by metals restricts the strength of the photoacoustic signals generated on metal surfaces and require

high power lasers. Secondly, laser-induced strain waves typically have only a small effect on the optical properties of a metal, making it challenging to detect them.

A promising approach to address these challenges involves the use of a resonance to enhance the detection. Recent studies have demonstrated the effectiveness of surface plasmon resonances in enhancing photoacoustic signals by exciting surface plasmon polaritons (SPPs) on gold gratings [24–28]. The excitation of SPPs leads to strong optical absorption, and a shift in the SPPs resonance induced by strain waves results in relatively large reflection changes. However, this method requires the creation of nanostructures and specific angles of incidence for SPP excitation [29,30]. It thus adds complexity and can be time-consuming, limiting practical applications.

In this paper, we propose a simple and efficient alternative approach to enhance and control photoacoustic signals, involving the use of ultra-thin semiconducting optical coatings on metal surfaces. These coatings are high-refractive-index, absorbing layers which provide a relatively sharp etalon resonance in the optical reflection as a function of semiconductor layer thickness. The effect of the layer is twofold. First, it boosts the light absorption in the system and strengthens the strain wave generation. Second, it provides a higher sensitivity of the optical reflection in response to small changes in optical thickness and/or change in the optical phase and amplitude of the optically reflected wave, induced by strain waves, thus improving detection. With a 12 nm thick layer of Ge on top of Au, we observe relatively large reflection changes induced by strain waves and achieve a 15-fold enhancement in the signal compared to the signals from Au without the Ge layer on top. Similarly, a 5 nm thick Si layer on Pt exhibits a signal enhancement by approximately a factor of two. Our approach is simple and less sensitive to the light incidence angle, making it more practical for real-world applications. Moreover, this approach can be used to enhance the optical absorption, requiring less pump power. In addition, properly choosing the pump wavelength gives some control over whether the light is predominantly absorbed in the metal or in the semiconductor layer. Our results show that ultra-thin semiconductor coatings can significantly enhance and provide some control over the photoacoustic response in metals, offering an accessible and straightforward method for improving photoacoustic signal strength.

2.   Sample preparation and characterization

To demonstrate the potential of semiconductor layers coated on metals in enhancing photoacoustic signals, we first prepared Ge-Au samples by depositing a ~75 nm thick Au layer on a 0.5 mm thick glass substrate using electron-beam-evaporation. On top of the Au layer, ten different thicknesses of Ge were deposited, ranging from 0-40 nm, with an increment of 4 nm. A photograph of the fabricated sample is shown in Fig. 1(a). The leftmost yellow color corresponds to bare Au, and the Ge layer thickness increases from left to right. The sample color is highly sensitive to the thickness of the Ge layer, already for modest thicknesses. It is due to the high refractive index of Ge and the non-trivial phase change upon reflection from the Ge-Au interface [31–33]. Note that the actual thickness of the Ge layers slightly varies from the labeled thickness due to inaccuracies in the thickness calibration of the deposition machine. Therefore, we performed SEM imaging on sample cross-sections for actual thickness measurements. The SEM images of the Ge-Au samples are shown in Supplement 1 Fig. S1.

To characterize the resonance, we measured reflection spectra from the Ge-Au samples in the wavelength range from 400-1000 nm using a white light source (Avantes, AvaLight-HAL-S-Mini) and spectrometer (Avantes AvaSpec-ULS2048x64TEC) at normal incidence. The reflection spectra are referenced with a reflection spectrum collected from Ag, which has a relatively flat reflection spectrum in the measured wavelength range. The resultant linear reflectivity curves as a function of wavelength, for the bare Au and for the Au with Ge layers on top, are plotted in Fig. 1(b) for different thicknesses of the Ge layer. The topmost yellow curve represents the reflection spectrum of bare Au which shows a low reflectivity at shorter wavelengths and a higher reflectivity towards longer wavelengths. In contrast, for Au with a Ge layer on top, a minimum in
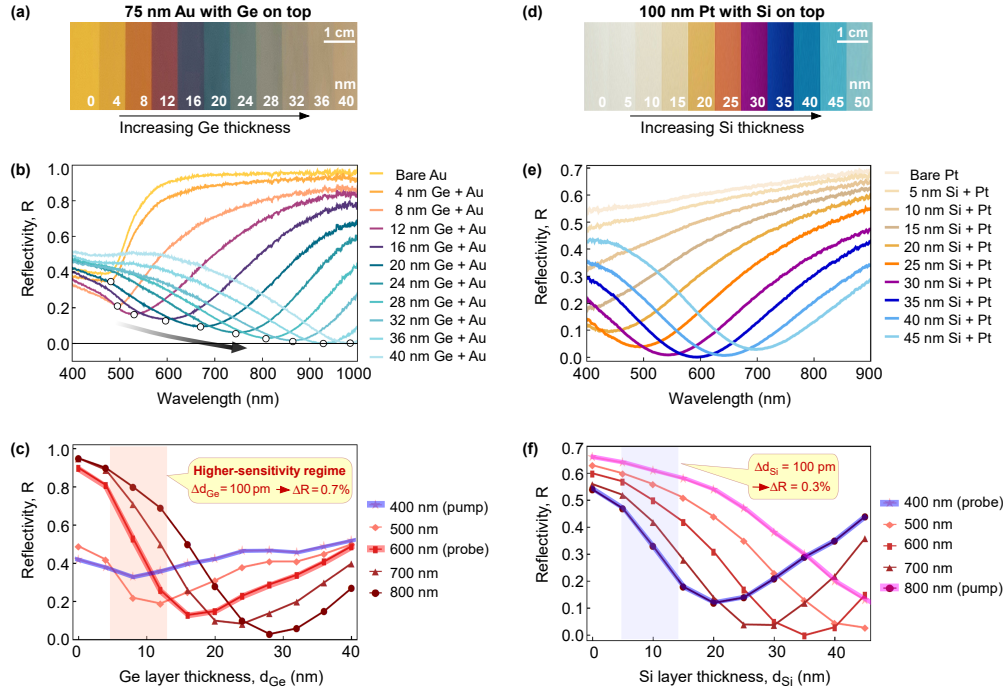
Fig. 1. Sample preparation and characterization. (a) Image of the prepared Ge-Au sample with different thicknesses of Ge deposited on Au. Optical interference produces the different colors. (b) Measured reflection spectra of the Ge-Au sample for various Ge thicknesses. Adding Ge on Au creates a dip in the reflection spectra. The minimum becomes deeper and shifts towards longer wavelengths with increasing thickness of the Ge layers. (c) Reflectivity curves of the Ge-Au samples as a function of Ge thickness d_{Ge} for different wavelengths. The pumping and probing wavelengths are highlighted in blue and red respectively. For 600 nm wavelength, a higher-sensitivity regime is shaded in red. Here, a small change of 100 pm in Ge thickness would result in a ~ 0.7% change in reflectivity. (d) Image of the fabricated Si-Pt sample. (e) Reflection spectra of the Si-Pt sample for various Si thicknesses. (f) Reflectivity curves of the Si-Pt samples as a function of Si thickness d_{Si} for different wavelengths. The curves corresponding to pump and probe wavelengths in the experiment are highlighted with magenta and blue colors respectively. For a wavelength of 400 nm, the blue shaded region is where a small change of 100 pm in Si thickness would result in a ~ 0.3% change in reflectivity.

the reflection spectrum (black circles) develops indicating an increased absorption in the system. This minimum becomes deeper and shifts towards longer wavelengths with increasing thickness of the Ge layers, eventually approaching 100% absorption for Ge layer thicknesses of 32 nm and higher. We note that this strong absorption is present only when the Ge is present on Au. Separately, neither the Au nor the 32 nm Ge give rise to 100% absorption. It is caused by the etalon effect whereby multiple reflections inside the Ge layer increase the optical interaction of the light with the Ge-Au system.

In Fig. 1(c), we plot the linear reflectivity for the Ge-Au sample against the thickness of Ge layer (d_{Ge}) for various light wavelengths. For each wavelength, we observe an etalon resonance where the reflectivity decreases significantly for a certain thickness of the Ge layer. Specifically, for a wavelength of 600 nm, a minimum occurs at a Ge thickness of around 16 nm. Notably, at the slope of the resonance, as indicated by the red shaded region, the sensitivity of reflection to small changes in the physical/optical thickness of Ge (Δd_{Ge}) is highest. For example, at a 600 nm wavelength, a small change of 100 pm in the Ge thickness, for example, would induce a change in reflectivity of approximately 0.7%. Our focus is on optimizing the probe signal for detecting strain waves within the Au layer, which is better achieved with thinner Ge coatings for which the slope of the reflection versus layer thickness is steeper, suggesting a higher sensitivity for strain-wave induced thickness changes. These thinner coatings show more absorption at wavelengths around 400 nm or 500 nm. Since our laser system readily provides a 400 nm wavelength, it is a practical choice for our experiments. Note that Fig. 1(c) shows maximum absorption around 800 nm, but only for the thicker Ge layers. For thicker Ge layers, the strain waves generated within the Ge layer itself would dominate, overshadowing the signal from the Au. For optimum strain wave generation in Ge, 800 nm would be a better choice for the pump wavelength.

We also fabricated Si-Pt samples by depositing Si layers of ten different thicknesses (0-50 nm with steps of 5 nm) onto 100 nm Pt on a glass substrate (Fig. 1(d)). SEM images of the Si-Pt samples are presented in Fig. S2 in the Supplement 1. The measured reflectivity of these Si-Pt samples as a function of wavelength is depicted in Fig. 1(e). The reflection spectrum of bare Pt shows a low reflectivity of about 55% at the shortest wavelengths, which gradually increases towards longer wavelengths. In contrast, Pt coated with thin Si layers displays a minimum in the reflection spectrum for increasing Si thickness, indicating an increase in absorption. This reflectivity minimum shifts towards longer wavelengths with increasing Si thickness and becomes more pronounced, eventually reaching almost 0% at a wavelength of 600 nm for a Si layer thickness of approximately 35 nm. Figure 1(f) displays the reflectivity of the Si-Pt sample as a function of Si layer thickness (d_{Si}) at different optical wavelengths. At a Si layer thickness of approximately 10 nm, a small change of 100 pm in Si layer thickness would induce a change in reflectivity of approximately 0.3% for a 400 nm wavelength (blue shaded region).

Note that our focus is on maximizing the probe's optical response to laser-induced strain waves, rather than achieving resonant reflectivity for the pump wavelength. It is important to realise that the thickness of the layer, and the choice of pump and probe wavelengths are not independent parameters. This means that when probe wavelength and material thickness have been optimised for maximum optical response to strain waves, tuning the pump would in some cases help in increasing the strain wave amplitude. In our setup, our choice of pump wavelength is limited to 400 nm and 800 nm, and we show that this already allows some control over whether the pump pulse is absorbed in the top layer or the metal. At 800 nm, absorption mainly occurs in the Pt layer, while at 400 nm, both Pt and Si layers absorb light (see supplementary Fig. S9). This allows for tailored light absorption in both the metal and semiconductor layers, demonstrating the flexibility and control of our approach and suggest that further improvements could be made in the future with a fully tunable pump.
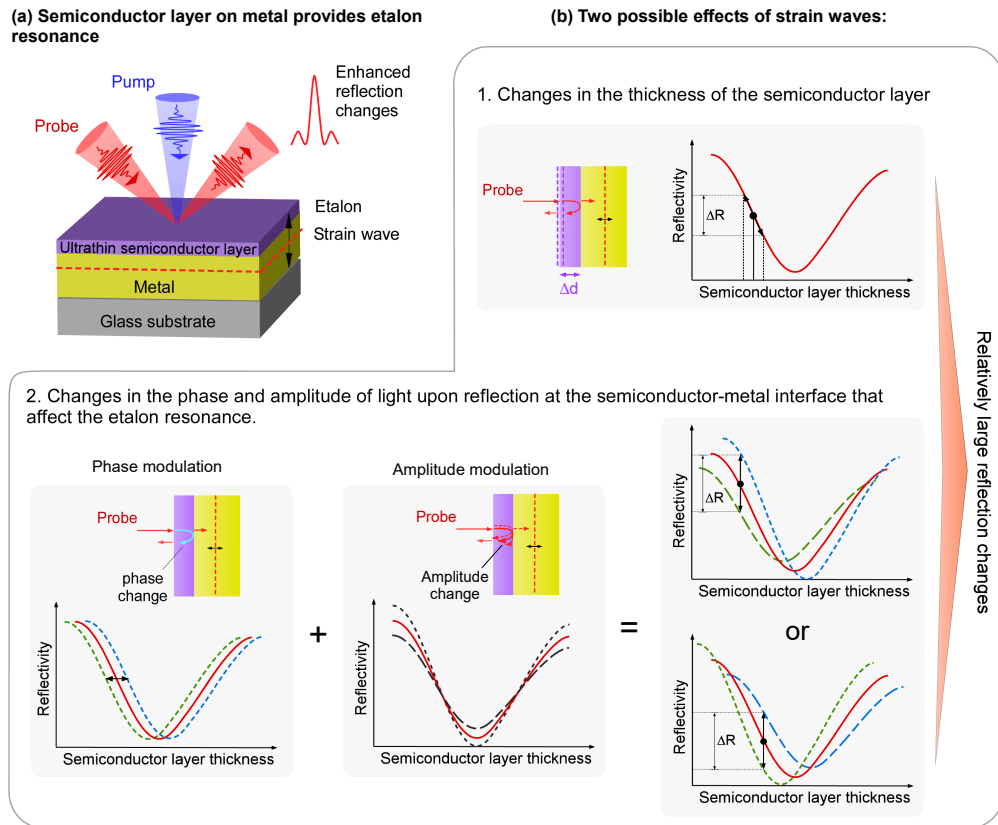
Fig. 2. **Enhancing photoacoustic signals using an etalon resonance** (a) Illustration of the semiconductor-metal system. The pump pulse induces a strain wave (red dotted line) influencing the optical properties. The induced changes are measured through changes in the probe beam reflection. (b) Two possible effects of the strain waves that result in relatively large reflection changes: 1) The expansion or contraction of the semiconductor layer. 2) Changes in the resonance due to phase and amplitude changes of the probe upon reflection at the semiconductor-metal interface.

The heightened sensitivity in reflection by probing at the slope of the resonance serves as the key mechanism for optically enhanced detection of photoacoustic signals and can be explained as follows. Figure 2(a) represents a schematic picture of the semiconductor-metal system. The pump pulse induces the strain wave that propagates within the system as represented by the red dotted line. The strain wave, being a density wave, affects the optical properties of the system and the induced changes can be probed by measuring the reflection of a probe beam. Two potential effects of the strain waves are illustrated in Fig. 2(b). They are 1. Expansion and contraction of the semiconductor layer caused by the strain wave. 2. Changes in phase and amplitude of the electric field of the probe upon reflection at the semiconductor-metal interface. The latter is caused by strain-wave-induced changes of the complex refractive index of the metal or semiconductor, leading to a change in the etalon resonance. The change in the phase of the probe upon reflection is equivalent to a lateral shift in the resonance curve while the change in the amplitude affects the resonance strength. The relative contributions of phase and amplitude-changes vary with semiconductor layer thickness. Small changes in the physical or optical thickness of the semiconductor layer, and/or a small changes in the resonance induced by strain waves, will lead to relatively large reflection changes when probing at the slope of

the resonance. It is worth noting that the semiconductor layers exhibit a resonance for layer thicknesses within a range of only a few to tens of nanometers. Due to their high refractive index (up to 5) and the non-trivial phase change upon reflection at the metal-semiconductor interface, these layers produce a steep slope in the reflectivity versus layer thickness. In contrast, low-refractive-index transparent materials like SiO_2 and Al_2O_3, when deposited on metals, show relatively weaker slopes in reflectivity curves, which reduces sensitivity, and these layers would also need to be thicker [34,35]. (see Supplement 1 Fig. S3 for details).
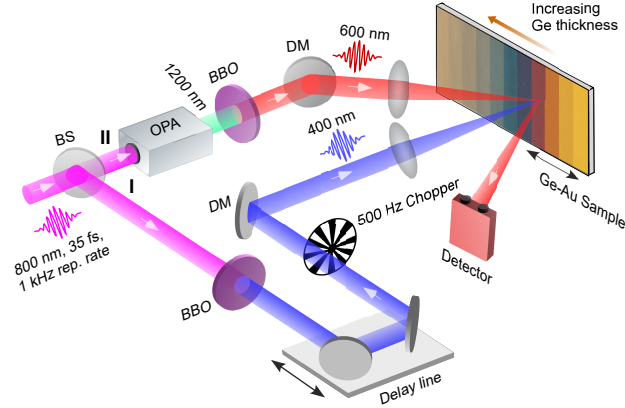
3.   Experimental setup

The experimental setups for the time-resolved photoacoustic measurements on Ge-Au and Si-Pt samples are illustrated in Fig. 3(a) and (b), respectively. The experiments use an amplified Ti:Sapphire femtosecond laser (Astrella, Coherent) with a central wavelength of 800 nm, a pulse width of 35 fs, a repetition rate of 1 kHz, and a maximum pulse energy of 6 mJ.

For the measurements on the Ge-Au samples, the laser beam is split into two beams using an 85:15 beam splitter, as shown in Fig. 3(a). The weaker 800 nm beam (I) passes through a frequency-doubling beta barium borate (BBO) non-linear optical crystal to generate a beam with a wavelength of 400 nm, and then through a variable optical delay line. The beam then passes through a 1 kHz mechanical chopper with a 50% duty cycle, synchronized with the laser. The chopper blocks every second pulse, thereby reducing the pulse repetition rate to 500 Hz. After reflecting from a dichroic mirror (DM), which filters out the residual 800 nm light, the beam is focused onto the sample at near normal incidence to a spot with a diameter of approximately 400 μm. This focused beam with a wavelength of 400 nm is used as the pump beam, and has a pulse energy of 3 μJ. The sample is mounted on a linear translation stage, so that samples with a different semiconductor coating thickness can be selected by translating it in the direction perpendicular to the pump beam propagation direction. The stronger 800 nm beam (II) is sent to an optical parametric amplifier (OPA, HE-TOPAS, from Light Conversion). The OPA generates laser pulses with a wavelength tunable between 1100-1500 nm, which are subsequently frequency doubled using a BBO crystal, creating pulses with wavelengths tunable between 550 nm and 750 nm. The generated pulses, with a 1 kHz repetition rate, have a bandwidth of ~15 nm (FWHM) and are used as a probe pulses. For our experiment, their wavelength is set to 600 nm. The probe laser pulses are focused onto the sample, overlapping with the pump beam, to a spot of around 100 μm diameter with an incident angle of approximately 20° with respect to the surface normal. The spot size of the probe beam at the sample is kept much smaller than the spot size of the pump beam to ensure that a reasonably uniformly pump-illuminated area is probed. The probe pulses have an energy of 25 nJ. The reflection of the probe pulse is measured using a Si photodiode. In the experiment, probe pulse reflection changes are measured as a function of the time-delay between the pump and the probe pulses.

For the measurements on the Si-Pt sample, the experimental setup (Fig. 3(b)) is slightly different. The stronger beam (II) passes through a mechanical chopper that reduces the repetition rate of the pulses to 500 Hz. The beam is focused onto the sample at near-normal incidence with a spot diameter of approximately 630 μm. This focused beam serves as a pump beam with a pulse energy of about 40 μJ. The weaker beam (I) passes through a frequency doubling BBO crystal and a variable optical delay line. After being reflected by a dichroic mirror (DM), the beam is focused onto the sample, with a spot diameter of approximately 280 μm at an angle of incidence of approximately 20°. The energy of the probe pulses is kept at ~100 nJ. A Si photodiode is used to measure the pump-induced reflection changes of the probe pulse.

(a) Experimental setup for Ge-Au measurements
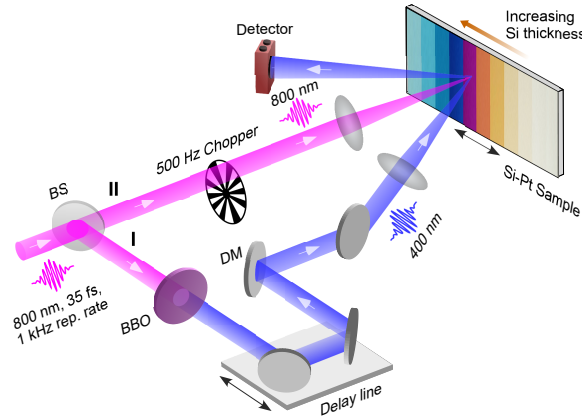
(b) Experimental setup for Si-Pt measurements

Fig. 3. Schematic of experimental setups for photoacoustic measurements on Ge-Au and Si-Pt samples. The femtosecond laser beam (800 nm) is split into two parts: the pump and probe beam. (a) For the measurements on the Ge-Au samples, the pump beam (I) is frequency-doubled to 400 nm using a BBO crystal and modulated at 500 Hz using a mechanical chopper. The probe beam (II) is directed through a three-stage OPA for parametric amplification, changing the wavelength to 1200 nm, which is further frequency-doubled using a BBO to 600 nm. Both pump and probe beams are focused onto the sample, and the time delay between them is controlled by a delay line. The reflection changes in the probe beam due to strain waves are measured with a silicon photodiode. (b) In measurements on the Si-Pt samples, the pump beam (II) is modulated at 500 Hz using a mechanical chopper, while the probe beam (I) is frequency doubled using a BBO crystal, to 400 nm. BS: Beam splitter, BBO: Beta barium borate, DM: Dichroic mirror.

4.   Results on enhancement of photoacoustic signals

We first performed measurements on Ge-Au samples and measured the probe pulse reflection changes as a function of time-delay between pump and probe pulse. We use pump and probe wavelengths of 400 nm and 600 nm with pulse energies of 3 μJ and 25 nJ respectively. At 400 nm, most of the absorbed light is absorbed by the Ge layer for thicknesses of 16 nm and higher. At 600 nm, this is true for all thicknesses and the penetration of the probe is largely confined to the Ge layer. The calculations of the optical absorption of the Ge-Au samples are shown in Fig. S4 of Supplement 1.

In Fig. 4(a), we plot the measured absolute reflection changes of the probe pulse, denoted as ΔR, as a function of the time-delay between the pump and probe pulses for various thicknesses of the Ge layer deposited on a ~75 nm thick Au layer. For all samples, a sharp reflection change (peak or dip) is seen at a time-delay of around 0 ps, caused by electron dynamics in the Ge-Au system. For longer delays, the plot exhibits some oscillatory changes in reflectivity, indicating the presence of strain waves. These oscillations are superimposed on a large exponentially decaying thermal background. The thermal background seems to decays gradually with a time constant of several nanoseconds.

To highlight the strain-wave-induced oscillations, we subtract the thermal background and plot the measured reflection changes as a function of time-delay between the pump and probe pulses in Fig. 4(b), for time-delays greater than 5 ps. Each curve represents reflection changes for a different thickness of Ge on the Au, with the Ge thickness increasing from top to bottom. Vertical offsets are given to each curve for clarity. The topmost curve represents reflection changes for bare Au. The bare Au displays a relatively weak pump absorption and exhibits weak oscillations, as shown in the top curve. However, a few nm thick Ge layer deposited on top of Au already enhances the signal, as can be seen in subsequent curves. For Ge thicknesses of 4, 8 and 12 nm, the oscillatory signal somewhat resembles a triangular wave with an amplitude that increases for thicker Ge layers.

The pump pulse initially heats up the electron gas. As electron-lattice coupling in Au is relatively weak compared to a metal like Pt, this leads to electron energy diffusion deeper into the Au layer, causing the Au layer to homogeneously heat up. Subsequently, the electron gas cools down by transferring heat to the lattice, inducing a periodic contraction and expansion of the layer. This causes periodic changes to the optical properties of the medium, leading to the observed oscillatory signal in the reflection. These oscillations have a period of approximately 50 ps. This corresponds to one round trip time of the strain waves inside the ~75 nm thick Au layer, as can be calculated using the longitudinal speed of sound in Au of 3240 m/s. For a Ge thickness of 16 nm and above the signal changes, featuring some rapid oscillations as well. Numerical simulations show that these rapid oscillations correspond to the high frequency strain waves generated inside the Ge layer itself or coupled from Au and bouncing back and forth inside the Ge layer. Details can be found in the Simulations section.

Given the existence of various oscillation frequencies, we performed a Fourier Transform of the thermal background-subtracted time-dependent signals. The frequency-dependent signal amplitudes are shown in Fig. 4(c) for different Ge layer thicknesses. Depending on the Ge thickness, various high frequency components in the frequency spectra are observed. Of particular interest is the low-frequency peak, denoted as P_{Au}, occurring at approximately 20 GHz. This peak is associated with the propagation of strain waves generated within the Au layer. These waves travel through the thickness of the Au layer, encounter the Au-glass interface, partially reflect back, and subsequently reach the Ge layer. Notably, this peak first intensifies with increasing thickness of the Ge layer, nearly vanishes when the Ge layer reaches a thickness of 16 nm, and then reemerges for thicker Ge layers.

To look at this in more detail, we restricted the frequency range to 10-30 GHz and filtered out the remaining frequencies. Subsequently, we performed an inverse Fourier transformation,
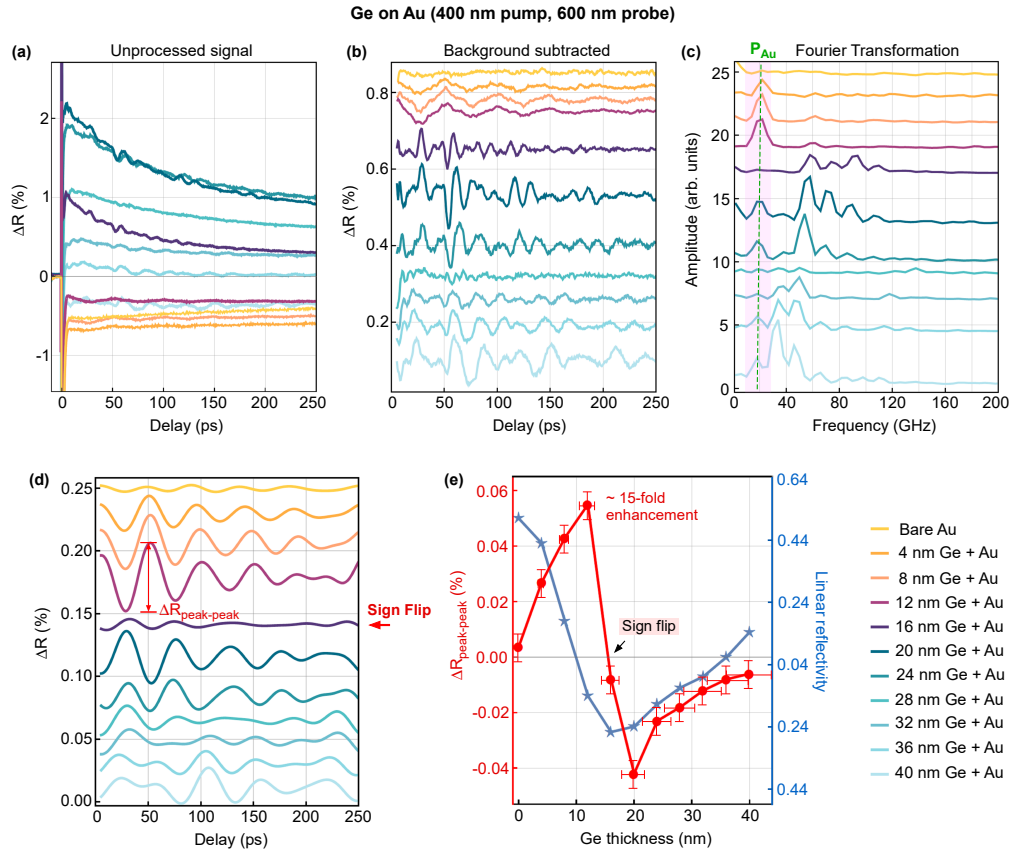
Fig. 4. Photoacoustic dynamics of Ge-Au system (a) Measured absolute reflection change of the probe pulse as a function of time-delay between the pump and probe pulses, for various thicknesses of the Ge layer deposited on Au. The vertical axis is meticulously zoomed in to provide a clearer visualization of the strain-induced oscillations present in the signal. (b) Background subtracted reflection changes as a function of time-delay between the pump and probe pulses for time-delays greater than 5 ps. A offset is added to each curve for clarity. (c) Fourier Transformations of the time-dependent signals plotted in (b). The shaded region around the peak frequency of 20 GHz, P_{Au}, corresponds to strain waves generated in Au. (d) Time-domain-signals after performing inverse-Fourier-transformation on only the highlighted frequency range (10-30 GHz) around the P_{Au} peak. Rest frequency spectra are filtered out. The oscillations flip sign around 16 nm Ge thickness. (e) Peak-to-peak amplitude of reflection changes, $\Delta R_{peak-peak}$, as a function of Ge layer thickness along with the measured linear reflectivity of the Ge-Au samples at a probe wavelength of 600 nm.

and the resulting time-domain signals are plotted in Fig. 4(d). The amplitude of the absolute reflection changes increases with increasing Ge thickness, particularly for Ge layer thicknesses of 4, 8 and 12 nm. Interestingly, the signals flip sign around a Ge layer thickness of 16 nm. For layers of 28 nm and thicker, the signals exhibit a bit more complex behavior.

As discussed before, the reflection sensitivity to optical thickness changes is expected to be highest at the slope of the etalon resonance. Therefore, reflection changes induced by strain waves are expected to be relatively large there. Moreover, the change in reflectivity is negative with increasing thickness for Ge layers on the falling edge of the resonance and become positive at the rising edge. To quantify this, we plot in Fig. 4(e) the peak-to-peak amplitude of the absolute reflection changes, $\Delta R_{peak-peak}$ (as labelled in Fig. 4(d)), as a function of Ge layer thickness (also shown in Fig. 1(c)). In the same figure, we plot the measured linear reflectivity as a function of Ge layer thickness, at the 600 nm probe wavelength. The strain-wave induced reflection changes first increase with Ge layer thickness, reaching a maximum enhancement factor of approximately 15 for a 12 nm thick layer of Ge, at the slope of the reflectivity versus Ge thickness curve. Then, the reflection change flips sign for a Ge layer thickness of 16 nm and above. This sign flip near the minimum of the reflectivity curve serves as strong evidence for the presence of an optical etalon effect in the photoacoustic measurements. Note that the maximum enhancement is not exactly at the location where the slope of the reflectivity curve is steepest, possibly because different thicknesses of Ge display a different amount of pump absorption, leading to some variation in the generated photoacoustic signal strength.

Measurements on the Ge-Au samples demonstrate the potential of optically enhancing the photoacoustic signals and generating high-frequency strain waves in the system using semiconductor coatings. The spectrum of high-frequency strain waves can be controlled by manipulating the thickness of the semiconductor layer. The enhancement and control of photoacoustic signals is further illustrated with measurements on Si-Pt samples which we will present below. Our calculations of the optical reflection of Ge-Au and Si-Pt samples indicate that by carefully selecting specific wavelengths for the pump and probe beams, and by adjusting the thickness of the semiconducting coating, it is possible to exert some control over the ratio of light absorbed in the metal and light absorbed in the semiconductor. Detailed calculations are provided in Supplement 1 in Fig. S8 and Fig. S9. The calculations specifically suggest that at a wavelength of 800 nm, nearly all light is absorbed by the Pt, with minimal absorption by the Si. This implies that strain wave generation predominantly takes place in the Pt when subjected to 800 nm pump light.

To explore the photoacoustic response of a Pt film coated with a Si layer, we first initiated strain waves using an 800 nm pump beam, and probed the sample at a wavelength of 400 nm. The pulse energies for the pump and probe pulses were set at 40 μJ and 100 nJ, respectively. Measured signals of the absolute reflection changes of the probe pulse (ΔR) as a function of time delay between the pump and probe are shown in Supplement 1 Fig. S5(a). In Fig. 5(a), we plot the background-subtracted absolute reflection changes of the probe pulse (ΔR) as a function of time delay between the pump and probe pulses, for various thicknesses of the Si layer deposited on ~100 nm of Pt. The topmost curve corresponds to the reflection change induced in bare Pt, while the subsequent curves correspond to reflection changes measured on samples with the Si layer thickness increasing from top to bottom. Each curve is vertically offset for clarity. Unlike the triangularly shaped signals for Au, we observe clearly separated echoes in the signal for Pt with a consistent period of 50 ps. This is due to the strong electron-lattice coupling in Pt which leads to the rapid cooling of the electron gas by transferring heat to the lattice. This initiates the generation of spatially and temporally shorter strain waves in Pt which propagate back and forth inside the Si-Pt system, resulting in periodic changes in the reflectivity. The round-trip time of these strain waves inside the ~100 nm thick Pt layer is approximately 50 ps, as can be calculated using the longitudinal speed of sound in Pt, of 3830 m/s. The reflection changes are

clearly enhanced with the ultra-thin layer of Si on top of Pt. For a Si layer of 5 nm thickness, the signal is already significantly improved. When the Si thickness reaches approximately 20 nm, the echoes become inverted. However, for Si layers thicker than 30 nm, the signal becomes more complex, with additional frequencies appearing. The complex nature of the signal for thicker layers of Si is related to the contribution of the strain-optic effect in the Si layer and is discussed later in the Simulation and Discussion section.
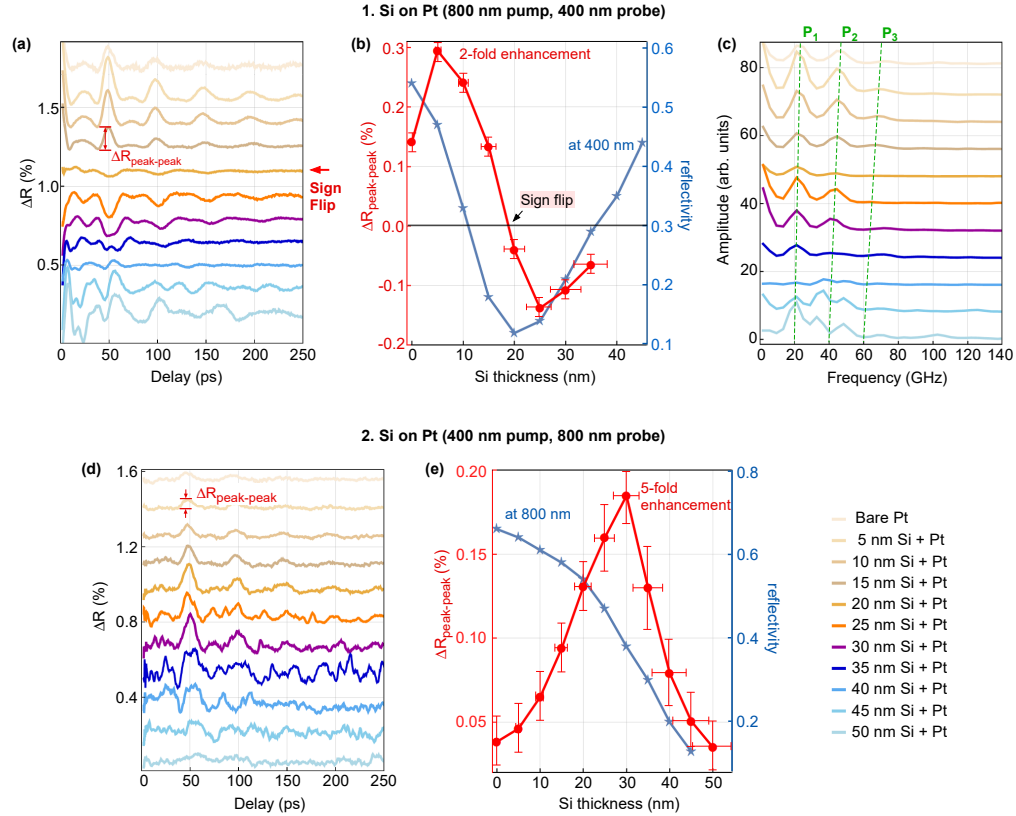

Fig. 5. Photoacoustic measurements on the Si-Pt system 1. Using 800 nm pump and 400 nm probe wavelengths (a) Background-subtracted reflection changes as a function of time-delay between the pump and probe pulses for time-delays greater than 5 ps. An offset is added to each curve for clarity. Oscillations flip their sign around a Si thickness of 20 nm. (b) Peak to peak amplitude of reflection changes, $\Delta R_{peak-peak}$, as a function of Si layer thickness along with the measured linear reflectivity of the Si-Pt sample at a probe wavelength of 400 nm. (c) Fast Fourier Transformations (FFTs) of the time-dependent signals. Dashed lines P_1, P_2 and P_3 highlight a decrease in the frequency of laser induced echoes for increasing thicknesses of the Si layer. **2. Using 400 nm pump and 800 nm probe wavelengths.** (d) Background-removed reflection changes as a function of time delay between the pump and probe pulses for time-delays greater than 5 ps. A offset is added to each curve for clarity. (e) Peak to peak amplitude of the reflection changes, $\Delta R_{peak-peak}$, as a function of Si layer thickness along with the linear reflectivity at a probe wavelength of 800 nm.

In Fig. 5(b) we plot the peak-to-peak amplitude of the absolute reflection changes, $\Delta R_{peak-peak}$, as a function of Si layer thickness along with the measured linear reflectivity of the Si-Pt sample for a probe wavelength of 400 nm, also shown in Fig. 1(f). Compared to the bare Pt, the optical

reflection changes are almost twice as large for Pt coated with a 5 nm thick Si layer. In addition, the sign of the echoes flips near the minimum of the linear reflectivity curve, as expected.

In Fig. 5(c), we plot the FFTs of the time-dependent signals. For thinner Si layers, spectral peaks around 20 GHz and its harmonics, are observed. The FFT's also show a small but significant decrease in the frequency of the laser-induced periodic signals for increasing thicknesses of the Si layer as indicated with the dashed lines P_1, P_2 and P_3. This is most likely the result of the increasing thickness of the Si-Pt stack with increasing Si layer thickness.

For comparison, we modified the experimental setup by reversing the roles of the pump and probe wavelengths and used 400 nm for pumping and 800 nm for probing. In this case the pump is absorbed by both the Pt and the Si and the probe only by the Pt. Energies and spot diameters of pump and probe pulses for these measurements were 5 μJ and 40 nJ, and 450 μm and 70 μm respectively. The measured probe pulse absolute reflection changes, ΔR, as a function of time-delay between the pump and probe pulses are shown in Supplement 1 in Fig. S5(b). The absolute reflection changes obtained after subtracting the background are presented in Fig. 5(d) for various thicknesses of the Si layer deposited on Pt. The topmost curve corresponds to the reflection changes for bare Pt and for the remaining curves, the thickness of the Si layer increases from top to bottom. Laser-induced strain waves with a period of 50 ps are observed in the uncoated Pt layer. With a 10 nm thick Si coating on the Pt, a significant enhancement of the signal by a factor of five is observed. The signal-to-noise ratio decreases for thicker layers of Si as the absolute reflection signal from the sample also goes down for thicker layers of Si on Pt. This is shown in Fig. 5(e) (blue curve) where we plot both the static, linear reflectivity of the Si-Pt system for 800 nm wavelength and the amplitude of the strain-wave-induced signal ($\Delta R_{peak-peak}$) as a function of Si layer thickness. With a Si coating thickness of up to 50 nm, and with a 800 nm probing wavelength, no sign flip is observed, in contrast to what we see when we pump at 800 nm and probe at 400 nm wavelengths. This is consistent with the observation that with 800 nm as a probe wavelength, we only measure reflection changes on the falling edge of the resonance curve (blue curve in Fig. 5(e)) resulting in the absence of a sign reversal for the echoes.

Additionally, Supplement 1 Fig. S6 displays the probe pulse reflection changes for various thicknesses of Si layers (without Pt) deposited directly on a glass substrate, as a function of the time delay between the pump and probe pulses. The results indicate the absence of detectable acoustic signals directly generated within the Si layers.

5. Simulations and discussion

The generation process of strain waves strongly depends on the material. In metals, the main mechanism is the thermoelastic effect [2,15]. After pump absorption, the lattice undergoes a rapid temperature increase inducing thermal stress that becomes a source of the strain waves. In metals, the Two Temperature Model is employed to analyze the evolution of the lattice temperature after ultrafast laser excitation [36]. In semiconductors, strain arises from laser-induced electron-hole plasma density and lattice temperature changes, with corresponding equations describing their dynamics [2,37].

The propagation of strain waves is modeled using the theory of linear elasticity, considering restoring, viscous, and source stresses. To calculate the reflectivity change induced by a strain wave we assume a linear dependence of the complex refractive index change on strain. Thermodynamic and elastic equations are solved using the finite-difference time-domain (FDTD) method [38]. The absorption profile of the pump and the reflectivity of the probe are calculated by the transfer matrix method [39]. This modeling approach has been effectively applied in a recent work [35] to study photoacoustic signal formation in systems with thin transparent films on metal layers, demonstrating the impact of optical effects and film thickness on the temporal signal shape. Details of the theoretical model and of the simulations are given in the Supplement 1.

The measured and simulated reflectivity changes in the Ge-Au system are shown in Fig. 6(a) and (b) respectively. The reflectivity change ΔR is formed by three contributions: strain-optic coupling in Au, strain-optic coupling in Ge, and strain-induced thickness change of the Ge layer. Since the strain-induced reflectivity changes are small and do not exceed 1 percent, the total reflectivity change can be approximated by a linear combination of these three contributions. Concerning the resonance phenomenon, the strain-induced thickness change of the Ge layer represents a movement along the reflectivity curve (effect 1 in Fig. 2(b)). The strain-optic coupling in the Au layer causes phase and amplitude changes in the reflection coefficient at the Ge-Au interface. This leads to phase and amplitude modulation of the reflectivity curve (effect 2 in Fig. 2(b)). Finally, the strain-optic coupling in the Ge layer changes both the optical path length within the Ge layer and the reflection coefficient at the Ge-Au interface. The optical path length change is equivalent to the thickness change of the Ge layer that corresponds to movement along the reflectivity curve (effect 1 in Fig. 2(b) while the change of reflection coefficient at the Ge-Au interface results in phase and amplitude modulation of the reflectivity curve (effect 2 in Fig. 2(b)). Thus, the strain-optic coupling in the Ge layer can be represented by a combination of the effects 1 and 2 in Fig. 2.
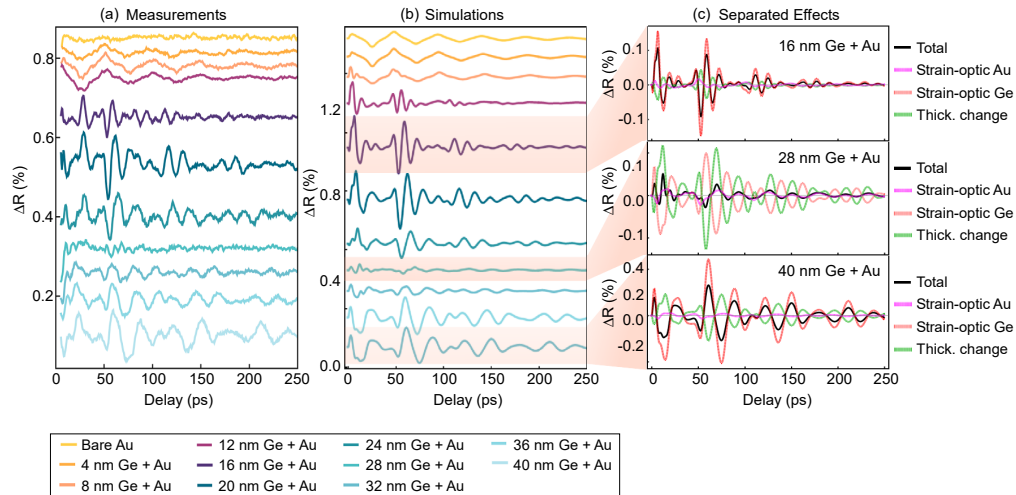

Fig. 6. Simulated absolute reflection change for Ge-Au system (a) and (b) show experimentally measured and simulated background-subtracted reflection changes for different thickness of Ge layer on Au respectively. (c) Simulated separated contributions of strain-optic coupling and strain-induced thickness change for three thicknesses of Ge, 16, 28 and 40 nm.

Simulated contributions of strain-optic coupling and strain-induced thickness change to the reflectivity change are plotted in Fig. 6(c) for three thicknesses of Ge; 16, 28 and 40 nm. To simplify the notation, we will call the three contributions of strain-optic coupling in Au, strain-optic coupling in Ge, and strain-induced thickness change of the Ge layer as Au-signal, Ge-signal, and d-signal respectively. In general, strain waves are generated in both the Ge and Au layers. Upon generation, the strain wave generated in Au propagates towards the back side of the sample but also partially couples into the Ge. The strain waves generated in Ge and those arriving from the Au, also bounce back and forth within the Ge layer and partially couple into the Au layer after each roundtrip. After the roundtrip in the Au layer, the strain waves reach the Ge-Au interface where they get reflected, and are partially coupled into the Ge layer. The reflected part appears in the Au-signal while the part coupled into Ge appears in the Ge- and d-signals. The Au-signal has a shape similar to that of the bare gold layer while the Ge- and

d-signals contain high-frequency oscillations. These oscillations come from the strain wave bouncing within the Ge layer. Accordingly, the period of oscillations is twice the sound roundtrip time in Ge. The factor of two comes from the different acoustic impedance mismatches at the Ge-air and Ge-Au interfaces. Upon reflection at the Ge-air interface, the strain wave flips polarity while for the reflection at the Ge-Au interface the polarity is unchanged. Thus, a strain wave returns to the same state after two roundtrips in the Ge layer.

Germanium layers of up to 12 nm thickness do not significantly affect the strain propagation in the sample compared to the bare gold layer. In such samples strain generation also occurs mostly in the Au layer resulting in a triangular shape of the ΔR signals. Even though the strain wave still couples into the Ge layer, Ge- and d-signals counteract each other due to the negative strain-optic coefficient of Ge. Such a destructive interference makes the Au-signal more evident. With an increase of the Ge thickness both generation and detection mostly happen in the Ge layer. This results in a predominance of Ge- and d-signals that determine the complex shape of ΔR for thicker layers of Ge. The results of the simulations show a reasonable match with the measurements.

Simulations of Si-Pt samples (Fig. 7) show similar results. Silicon is almost not absorptive for 800 nm. Hence, the generation of strain waves happens only in platinum for all thickness of Si used here. The contribution of the strain in the Si layer becomes evident for thicker layers compared to Ge-Au samples. Furthermore, the strain coupling to the Si layer was not included for Si thicknesses below 20 nm, because this gave rise to a better agreement with experiments.
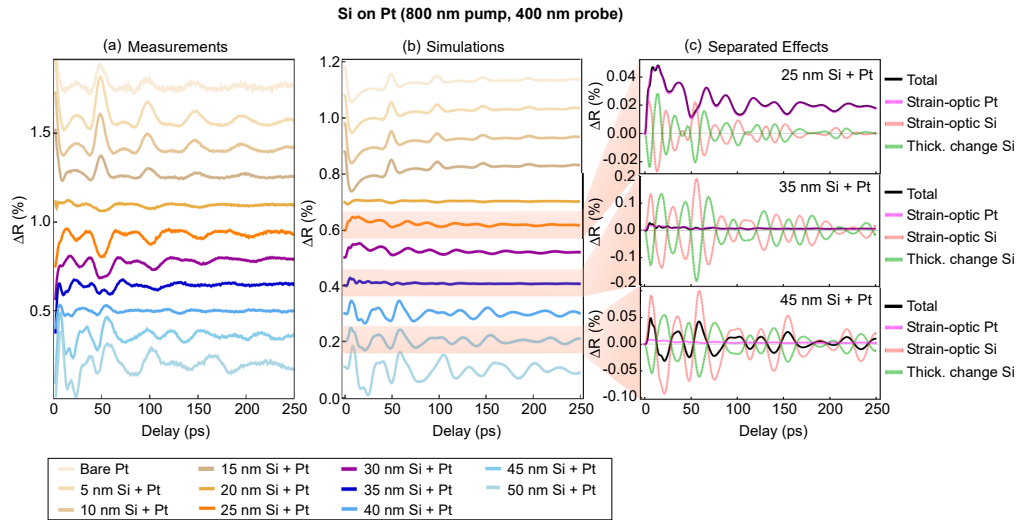

Fig. 7. Simulated absolute reflection change for Si-Pt system (a) and (b) show experimentally measured and simulated background-subtracted reflection changes for different thickness of Si layer on Pt respectively. (c) Simulated separated contributions of strain-optic coupling and strain-induced thickness change for three thicknesses of Si: 25, 35 and 45 nm.

6.   Conclusion

We investigated the impact that the incorporation of an ultra-thin high refractive index semiconductor layer on top of a metal surface has on photoacoustic signal detection. Our findings demonstrate that the addition of a semiconductor layer on a metal induces an etalon resonance in the system. Having a complex refractive index with a high value for the real part, the first minimum in the etalon reflectivity as a function of layer thickness already occurs for layer thicknesses of a few tens of nanometers. This results in a steep slope of the reflectivity versus

(optical) layer thickness and, thus, in larger changes in the optical reflectivity induced by the strain waves. The introduction of a semiconductor layer boosts optical reflectivity changes induced by weak pump-induced strain waves that are challenging to observe on bare metal surfaces. Interestingly, we observed a sign inversion in the signal after a certain thickness of the semiconductor layer, confirming the presence of the etalon resonance effect in our measurements. Furthermore, our study reveals the presence of fast oscillations for specific thicknesses of the semiconductor layer that correspond to strain waves generated within the semiconductor layer itself. It suggests that for research applications thin semiconductor layers may also be used as transducers to detect and generate high-frequency strain waves for applications requiring high spatial resolution. In addition, a proper choice of semiconductor coating thicknesses and pump-probe wavelengths in our approach, offers an increased control over absorption, creating some flexibility to customize light absorption in both the metal and the semiconductor. This method offers a simple and effective way to improve and advance photoacoustic measurements.

Disclosures. The authors declare no conflicts of interest.

Data availability. The data supporting the findings of this study are available from the corresponding author upon reasonable request.

Supplemental document. See Supplement 1 for supporting content.

References

1. C. Thomsen, J. Strait, Z. Vardeny, *et al.*, "Coherent phonon generation and detection by picosecond light pulses," Phys. Rev. Lett. **53**(10), 989–992 (1984).
2. C. Thomsen, H. T. Grahn, H. J. Maris, *et al.*, "Surface generation and detection of phonons by picosecond light pulses," Phys. Rev. B **34**(6), 4129–4138 (1986).
3. P. Ruello and V. E. Gusev, "Physical mechanisms of coherent acoustic phonons generation by ultrafast laser action," Ultrasonics **56**, 21–35 (2015).
4. T. F. Crimmins, A. Maznev, and K. A. Nelson, "Transient grating measurements of picosecond acoustic pulses in metal films," Appl. Phys. Lett. **74**(9), 1344–1346 (1999).
5. R. Tobey, M. Siemens, M. Murnane, *et al.*, "Transient grating measurement of surface acoustic waves in thin metal films with extreme ultraviolet radiation," Appl. Phys. Lett. **89**(9), 091108 (2006).
6. B. Daly, N. Holme, T. Buma, *et al.*, "Imaging nanostructures with coherent phonon pulses," Appl. Phys. Lett. **84**(25), 5180–5182 (2004).
7. A. Antoncecchi, H. Zhang, S. Edward, *et al.*, "High-resolution microscopy through optically opaque media using ultrafast photoacoustics," Opt. Express **28**(23), 33937–33947 (2020).
8. B. Audoin, "Principles and advances in ultrafast photoacoustics; applications to imaging cell mechanics and to probing cell nanostructure," Photoacoustics **31**, 100496 (2023).
9. Y. Wong, R. Thomas, and G. Hawkins, "Surface and subsurface structure of solids by laser photoacoustic spectroscopy," Appl. Phys. Lett. **32**(9), 538–539 (1978).
10. M. W. Sigrist, "Trace gas monitoring by laser photoacoustic spectroscopy and related techniques (plenary)," Rev. Sci. Instrum. **74**(1), 486–490 (2003).
11. D. Schneider, T. Witke, T. Schwarz, *et al.*, "Testing ultra-thin films by laser-acoustics," Surf. Coat. Technol. **126**(2-3), 136–141 (2000).
12. J. Arlein, S. Palaich, B. Daly, *et al.*, "Optical pump-probe measurements of sound velocity and thermal conductivity of hydrogenated amorphous carbon films," J. Appl. Phys. **104**(3), 033508 (2008).
13. H. Zhang, A. Antoncecchi, S. Edward, *et al.*, "Unraveling phononic, optoacoustic, and mechanical properties of metals with light-driven hypersound," Phys. Rev. Appl. **13**(1), 014010 (2020).
14. B. Perrin, B. Bonello, J.-C. Jeannet, *et al.*, "Picosecond ultrasonics study of metallic multilayers," Phys. B **219-220**, 681–683 (1996).
15. O. B. Wright, "Ultrafast nonequilibrium stress generation in gold and silver," Phys. Rev. B **49**(14), 9985–9988 (1994).

16. V. E. Gusev and O. B. Wright, "Ultrafast nonequilibrium dynamics of electrons in metals," Phys. Rev. B **57**(5), 2878–2888 (1998).
17. G. Tas and H. J. Maris, "Electron diffusion in metals studied by picosecond ultrasonics," Phys. Rev. B **49**(21), 15046–15054 (1994).
18. M. R. Armstrong, E. J. Reed, K.-Y. Kim, *et al.*, "Observation of terahertz radiation coherently generated by acoustic waves," Nat. Phys. **5**(4), 285–288 (2009).
19. V. Verrina, S. Edward, H. Zhang, *et al.*, "Role of scattering by surface roughness in the photoacoustic detection of hidden micro-structures," Appl. Opt. **59**(30), 9499–9509 (2020).
20. S. Edward, H. Zhang, I. Setija, *et al.*, "Detection of hidden gratings through multilayer nanostructures using light and sound," Phys. Rev. Appl. **14**(1), 014015 (2020).
21. V. Verrina, S. Edward, H. Zhang, *et al.*, "Photoacoustic detection of low duty cycle gratings through optically opaque layers," Appl. Phys. Lett. **117**(5), 051104 (2020).
22. R. J. Smith, F. P. Cota, L. Marques, *et al.*, "Optically excited nanoscale ultrasonic transducers," J. Acoust. Soc. Am. **137**(1), 219–227 (2015).
23. G. Wissmeyer, M. A. Pleitez, A. Rosenthal, *et al.*, "Looking at sound: optoacoustics with all-optical ultrasound detection," Light: Sci. Appl. **7**(1), 53 (2018).
24. V. V. Temnov, "Ultrafast acousto-magneto-plasmonics," Nat. Photonics **6**(11), 728–736 (2012).
25. G. De Haan, V. Verrina, A. J. Adam, *et al.*, "Plasmonic enhancement of photoacoustic-induced reflection changes," Appl. Opt. **60**(24), 7304–7313 (2021).
26. G. De Haan, E. Abram, T. van den Hooven, *et al.*, "Plasmonic enhancement of photoacoustic strain-waves on gold gratings," AIP Adv. **12**(2), 025227 (2022).
27. T. J. van den Hooven and P. C. Planken, "Surface-plasmon-enhanced strain-wave-induced optical diffraction changes from a segmented grating," Photoacoustics **31**, 100497 (2023).
28. F. Noll, N. Krauß, V. Gusev, *et al.*, "Surface plasmon-based detection for picosecond ultrasonics in planar gold-dielectric layer geometries," Photoacoustics **30**, 100464 (2023).
29. N. Rotenberg, J. N. Caspers, and H. M. van Driel, "Tunable ultrafast control of plasmonic coupling to gold films," Phys. Rev. B **80**(24), 245420 (2009).
30. R. H. Ritchie, E. Arakawa, J. Cowan, *et al.*, "Surface-plasmon resonance effect in grating diffraction," Phys. Rev. Lett. **21**(22), 1530–1533 (1968).
31. M. A. Kats and F. Capasso, "Ultra-thin optical interference coatings on rough and flexible substrates," Appl. Phys. Lett. **105**(13), 131108 (2014).
32. M. A. Kats, R. Blanchard, P. Genevet, *et al.*, "Nanometre optical coatings based on strong interference effects in highly absorbing media," Nat. Mater. **12**(1), 20–24 (2013).
33. Y. J. Yoo, G. J. Lee, K.-I. Jang, *et al.*, "Fabrication of ultra-thin color films with highly absorbing media using oblique angle deposition," JoVE **29**, e56383 (2017).
34. H. Zhang, A. Antoncecchi, S. Edward, *et al.*, "Enhancing the detection of laser-excited strain waves via transparent nanolayers," Phys. Rev. B **104**(20), 205416 (2021).
35. M. Illienko, M. C. Velsink, and S. Witte, "Understanding photoacoustic signal formation in the presence of transparent thin films," Photoacoustics **38**, 100617 (2024).
36. S. Edward, A. Antoncecchi, H. Zhang, *et al.*, "Detection of periodic structures through opaque metal layers by optical measurements of ultrafast electron dynamics," Opt. Express **26**(18), 23380–23396 (2018).
37. O. Wright and V. Gusev, "Acoustic generation in crystalline silicon with femtosecond optical pulses," Appl. Phys. Lett. **66**(10), 1190–1192 (1995).
38. K. Yee, "Numerical solution of initial boundary value problems involving maxwell's equations in isotropic media," IEEE Transactions on antennas and propagation 14, 302–307 (1996).
39. S. J. Byrnes, "Multilayer optical calculations," arXiv (2020).